REVIEWS

Comprehensive, *in operando*, and correlative investigation of defects and their impact on device performance

Yong Zhang[1, †] and David J. Smith[2, †]

[1]Electrical and Computer Engineering Department, University of North Carolina at Charlotte, Charlotte, NC 28223, USA

[2]Department of Physics, Arizona State University, Tempe, Arizona 85287, USA

Abstract: Despite the long history of research that has focused on the role of defects on device performance, the studies have not always been fruitful. A major reason is because these defect studies have typically been conducted in a *parallel* mode wherein the semiconductor wafer was divided into multiple pieces for separate optical and structural characterization, as well as device fabrication and evaluation. The major limitation of this approach was that either the defect being investigated by structural characterization techniques was not the same defect that was affecting the device performance or else the defect was not characterized under normal device operating conditions. In this review, we describe a more comprehensive approach to defect study, namely a *series* mode, using an array of spatially-resolved optical, electrical, and structural characterization techniques, all at the individual defect level but applied sequentially on a fabricated device. This novel sequential approach enables definitive answers to key questions, such as: (i) how do individual defects affect device performance? (ii) how does the impact depend on the device operation conditions? (iii) how does the impact vary from one defect to another? Implementation of this different approach is illustrated by the study of individual threading dislocation defects in GaAs solar cells. Additionally, we briefly describe a 3-D Raman thermometry method that can also be used for investigating the roles of defects in high power devices and device failure mechanisms.

1. Introduction

Defects in semiconductors consist of two major types, namely, point defects and extended defects[1−4]. Types of point defects include substitutional or interstitial foreign atoms, vacancies, anti-sites, or their complexes, and these defects usually involve one or a few atoms at most. Conversely, extended defects, such as threading dislocations or grain boundaries, can involve thousands or more atoms that are displaced from their regular lattice sites. One distinct difference between the two types of defects lies in that one single extended defect may exhibit much higher density of states than that of many point defects jointly for a moderate level of point defects. Since point defects can often be saturated with high carrier density, they will have greater impact for applications involving low carrier densities, whereas extended defects will be more detrimental for high carrier density applications[5, 6]. In practice, these two defect types will often play competing roles in a device. For example, increased carrier density may lead to larger carrier diffusion lengths, which will worsen the adverse effects of extended defects, since they may deplete a large number of carriers within the diffusion length[5, 7]. In addition, point defects typically degrade device performance, whereas extended defects will not only have the same effect but they may also be responsible for the ulti-mate, fatal device failure. Empirical correlations between the formation of so-called dark-line defects and degradation of GaAs semiconductor lasers were reported decades ago[8]. However, obtaining direct evidence is usually more difficult. It was shown recently that a simple dislocation defect could mutate under high-density optical injection conditions into a far more detrimental dark-line defect[5]. Neverthless, it still remains to be shown how the defect mutates under electrical injection in a practical device.

There are many different methods available for characterizing the structure and properties of individual defects correlatively[5, 9−19]. In particular, advanced microscopy techniques can nowadays provide detailed knowledge about structural defects in semiconductor materials and devices. Nevertheless, carrying out *operando* characterization at an individual defect level is often highly challenging or even impossible. Thus, determining the impact of specific types of defects on device performance and failure mechanisms is rarely answered systematically nor unambiguously. Some open questions include the following:

(i) How is device performance affected by an individual defect? Many such defects, including their atomic structure, can be imaged but the defects are typically not studied in functioning devices.

(ii) In what way does the impact of the defect depend on the device operation conditions? For instance, some defect types are likely to be more problematic at low carrier density, whereas others might be more detrimental at high carrier density. Such conditions could, for example, apply to a solar

Correspondence to: Y Zhang, yong.zhang@uncc.edu; D J Smith, dsmith1@asu.edu
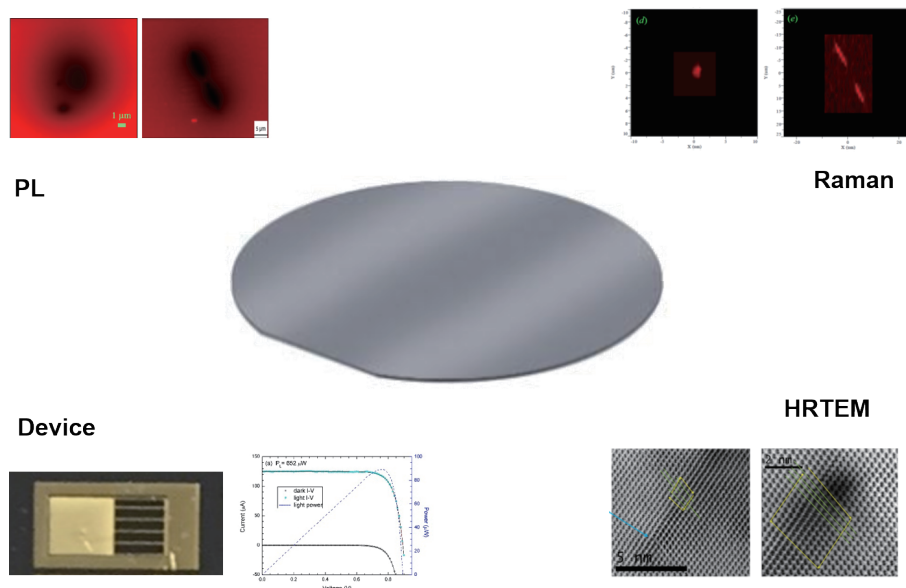
Fig. 1. (Color online) The parallel mode of defect characterization – wafer is cut into pieces for separate studies. Examples used are only for demonstration purposes. They are not necessarily obtained from the same wafer.

cell operating at one sun vs. 1000 suns or to an LED operating at 10 mA vs. 1000 mA.

(iii) How does the impact vary from one defect to another? One specific type of defect might be thought to be worse than another, but it is impractical to construct specific defects with known microscopic structure in a device and then compare their impact.

This type of information would enable a much more concrete understanding of the crucial role of defects in device operation, particularly providing the knowledge for assessing the need and possible strategies for removing or mitigating their impact.

Despite the long history of semiconductor defect research, the efforts have not always been very effective. Defect studies have mostly been performed in a *parallel mode.* One wafer is divided into multiple pieces used separately for structural, optical, and electrical characterization, as well as device fabrication and testing, as illustrated in Fig. 1: confocal photoluminescence (PL) imaging in one piece identified some defects that quenched the PL signal; high-resolution Raman imaging in another piece showed enhanced Raman signal at certain defect sites; high-resolution transmission electron microscopy (HRTEM) in yet another piece observed a dislocation defect and determined its detailed structure; and one more piece was fabricated into a solar cell on which an individual defect was located, for example by PL imaging, and this defect was further found to significantly reduce the photovoltaic efficiency when a laser beam was focused at the defect location. This commonly adopted approach of defect study clearly yields a lot of interesting information about the defects present in a particular material, and the general practice appears to be efficient. Unfortunately, it is incapable of yielding conclusive information about how the specific defects might affect the device performance or provide definitive answers to the crucial questions posed above. The major limitation of this approach is that either the defect investigated by structural characterization techniques is not the same defect that is affecting the device performance (i.e., they are presumed to be similar defects but are nev-

ertheless taken from different pieces of the material) or the defect is not characterized under normal device operating conditions.

There are in fact many well-known defect characterization techniques that provide qualitative assessments of material quality, such as chemical etching where the observed etch pit density is used as a measure of defect density and often correlates well qualitatively with device performance. However, it is usually unclear what effects a defect corresponding to a specific etch pit would have if the material were used for fabricating a real device, for instance, a solar cell. Attempting to address this question, we decided to correlate PL imaging, chemical etching, and scanning electron microscopy (SEM) imaging of CdTe epilayers by carrying out the measurements in the same order as they are mentioned[13]. Interestingly, it was observed that the PL dark spot density was much higher than the etch pit density. It was tempting to explain the discrepancy between the two densities in terms of the difference in sensitivity of the two techniques. However, unexpectedly, despite the lower density, etch pits did not always match the locations of the dark spots visible in PL imaging[13]. These findings suggest the need to determine which defects are actually impactful in a real device. Although the PL imaging results in this specific study were somewhat closer to the effect of defect recombination in real devices, the PL process is in general unable to reveal how carriers are generated, injected, or extracted in real electronic or optoelectronic devices, such as transistors, photo-detectors, solar cells, and LEDs.

This background has inspired us to embrace a more comprehensive approach to defect study, namely applying an array of correlative and spatially-resolved optical, electrical, and structural characterization techniques, all at the individual defect level but applied sequentially, i.e., in a *series mode*[20, 21], as illustrated in Fig. 2. Specifically, after a device is fabricated, individual defects on the device are identified. Then, the impact of individual defects is thoroughly investigated by applying different techniques as needed in a proper order, such as electroluminescence (EL), PL, micro-Raman, and micro-scale il-
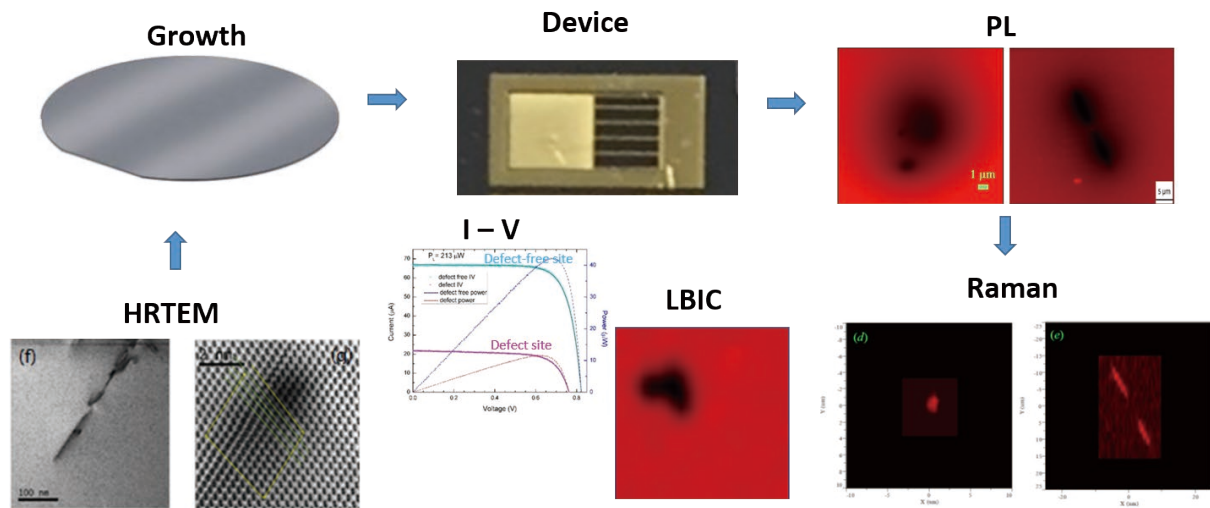
Fig. 2. (Color online) Series mode of defect study. Examples used are only for demonstration purposes. They are not necessarily obtained from the same device.

luminated current–voltage (I–V) measurements[22]. As the last step, the atomic-scale defect structures for the same defects are determined using HRTEM. It has been shown previously that defects may be modified or mutate during device operation[8, 23] or under high density photo-excitation[5]. To investigate defects in their as-grown states, care should be taken to avoid unintended modifications to the defect structure by limiting the illumination light density or injection current level to below any mutation thresholds, so that the native defect structure can be obtained by HRTEM. Our past efforts were in this category. On the other hand, for the purpose of investigating the possible role of the defects in the device failure mechanism, one can instead monitor the material properties and device characteristics at the defect sites (e.g., local spectroscopy signature, I–V characteristic under illumination, temperature) by continuously increasing the carrier injection level to reach the critical point.

In this focused review, we describe some examples from our recent work[20] to illustrate how *in operando* and correlative characterization at the single defect level, but implemented in the *series mode*, can provide not only a comprehensive understanding of the defect at a fundamental level but also unprecedented insight into the real impact of an individual defect on a real device (e.g., a GaAs solar cell). The findings enable us to explicitly answer those questions above that are otherwise impossible to address in the traditional parallel approach to defect characterization. We will also comment on an *in operando* micro-Raman 3-D thermometry approach[24] that can be used for providing a high-spatial resolution probe of high power semiconductor devices with high-temperature accuracy, such as LED and power electronic devices, and further expand the capability of the general approach.

2. Demonstration using GaAs solar cells

2.1. Identification of isolated defects in a finished device

Because of the relatively low density of dislocation defects (on the order of 10^3 cm^{-2} or lower) in the GaAs epilayer, it is inefficient and even challenging to identify individual defects using PL via raster scan. In a simple GaAs double hetero-

structure (DH) sample (e.g., GaInP/GaAs/GaInP), a PL imaging system was normally used to first identify the approximate locations of individual defects over a macroscopic area in the sample[5, 25]. Then, high-spatial-resolution PL mapping was used to determine its accurate location, followed by detailed optical investigation. However, in the finished device (the details of the device structure can be found in the original paper[20]), the PL signal from the active layer (i.e., the absorber), which was the layer of the main interest, typically became much weaker than that in the simple DH sample. The primary reason for the weakened PL signal was that the n$^+$p GaAs junction depleted the photo-generated minority carriers in the p-region or the active layer, which made it more difficult even using the PL imaging technique to locate individual defects. EL imaging was instead used for surveying a large device area, because it typically provided higher sensitivity and efficiency in locating individual defects that were detrimental to the electrically injected or photogenerated carriers. As shown in Fig. 3(a), EL imaging located a few potential threading dislocation defects (labelled as A, B, C) that exhibited quenched EL emission on a cell area named #5-2 (#5 for cell number, #5-2 for one cell area separated by electrode fingers). To ensure that these sites were not due to some unintended surface blemishes, we compared the EL image with an optical image Fig. 3(b), which indicated that the observed dark features in the EL image (indicated by the red dots in the optical image) were not surface effects but were generated from the interior of the sample. In this area, some surface blemishes were visible Fig. 3(b), which were actually unintended carbon-like parasitic depositions that did not match the exact defect locations[20]. Once the approximate defect locations were identified, they could be interrogated more closely using various high-resolution optical characterization techniques.

2.2. High resolution optical characterization of individual defects

Observations with high-resolution PL and Raman mapping scans were then used to confirm that the suspects located by EL imaging are indeed dislocation defects, because dislocation defects tend to exhibit certain distinctive features in PL and Raman[5, 26]. Fig. 3(c) shows the PL mapping result at the PL peak wavelength of a general site (~868 nm) near the
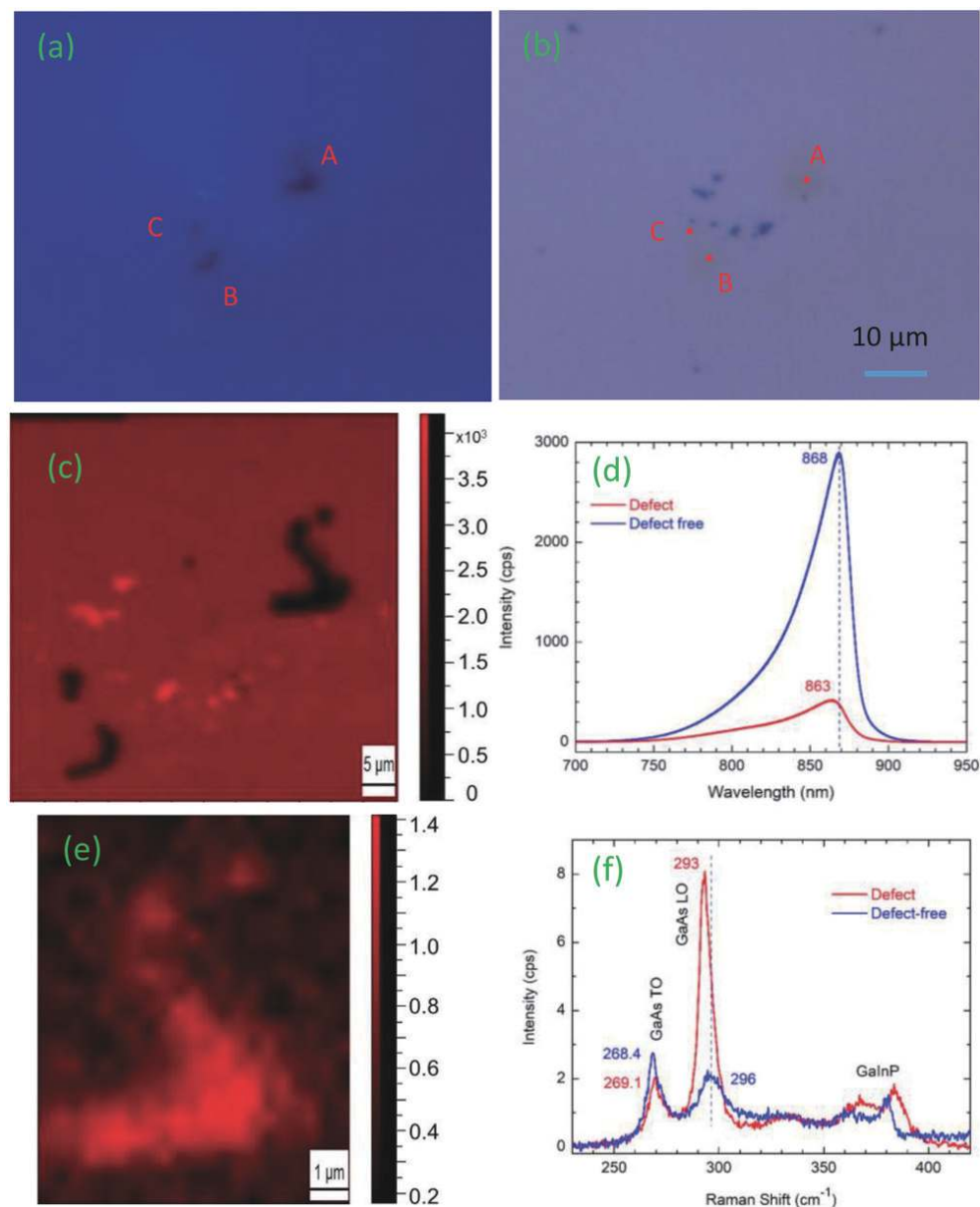
Fig. 3. (Color online) Correlative optical characterization of dislocation defects in a GaAs solar cell. (a) EL image using a 50×/NA0.5 LWD lens for device #5-2, showing a cluster of defects. (b) Optical image of the same area of (a) where red dots indicate defect locations. (c) PL mapping near the defect cluster using a 100×/NA0.9 lens with beam size approximately shown by the size of the red dot in (b). (d) PL spectra from typical defect-free location and the largest defect (#5-2A), under an excitation density of 5.6 × 10^4 W/cm^2. (e) Raman mapping near the largest defect (#5-2A). (f) Raman spectra from a typical defect-free location and the largest defect in (e). (reproduced with permission[20])

triplet in Fig. 3(a), with the comparison between the PL spectra of the largest defect site (#5-2A) and a general site given in Fig. 3(d), under an excitation density of 5.6 × 10^4 W/cm^2. As expected, the PL intensity is much weaker at the defect site than the general sites. Interestingly, at the defect site the PL peak energy is found to be blue-shifted to 863 nm compared to 868 nm at a general site. This finding is fairly common to similar defects observed in this and other GaAs samples, although the amount of peak shift varies. The possible reason for the shift could be the existence of a compressive in-plane strain field in the vicinity of the defect, although exact mechanism remains unclear. Fig. 3(e) shows Raman mapping result near the largest defect #5-2A at the peak position of the defect site, together with Raman spectra from the defect site and a defect-free site, shown in Fig. 3(f), measured un-

der the same condition as for the PL mapping. The defect-free site shows two GaAs Raman modes: 296 cm^{-1} for longitudinal optical (LO) mode and 268.4 cm^{-1} for transverse optical (TO) mode, while the defect Raman shows a sharper, stronger and red-shifted LO mode at ~293 cm^{-1} and a slightly weaker TO mode at 269.1 cm^{-1}. Note that the intrinsic GaAs Raman modes are reported to be 268.1 (TO) and 291.4 cm^{-1} (LO)[27] and our measurements for a GaAs: Cr sample yielded 268.0 and 291.5 cm^{-1}. At the first glance, the Raman results were counter intuitive: the spectrum of the defect site is closer to that of the intrinsic GaAs. In fact, the differences in intensity and frequency shift of the LO Raman mode can be attributed to the difference in carrier density between the defect and defect-free sites[26]: because the above-bandgap excitation generates an electron plasmon and the measured Ra-
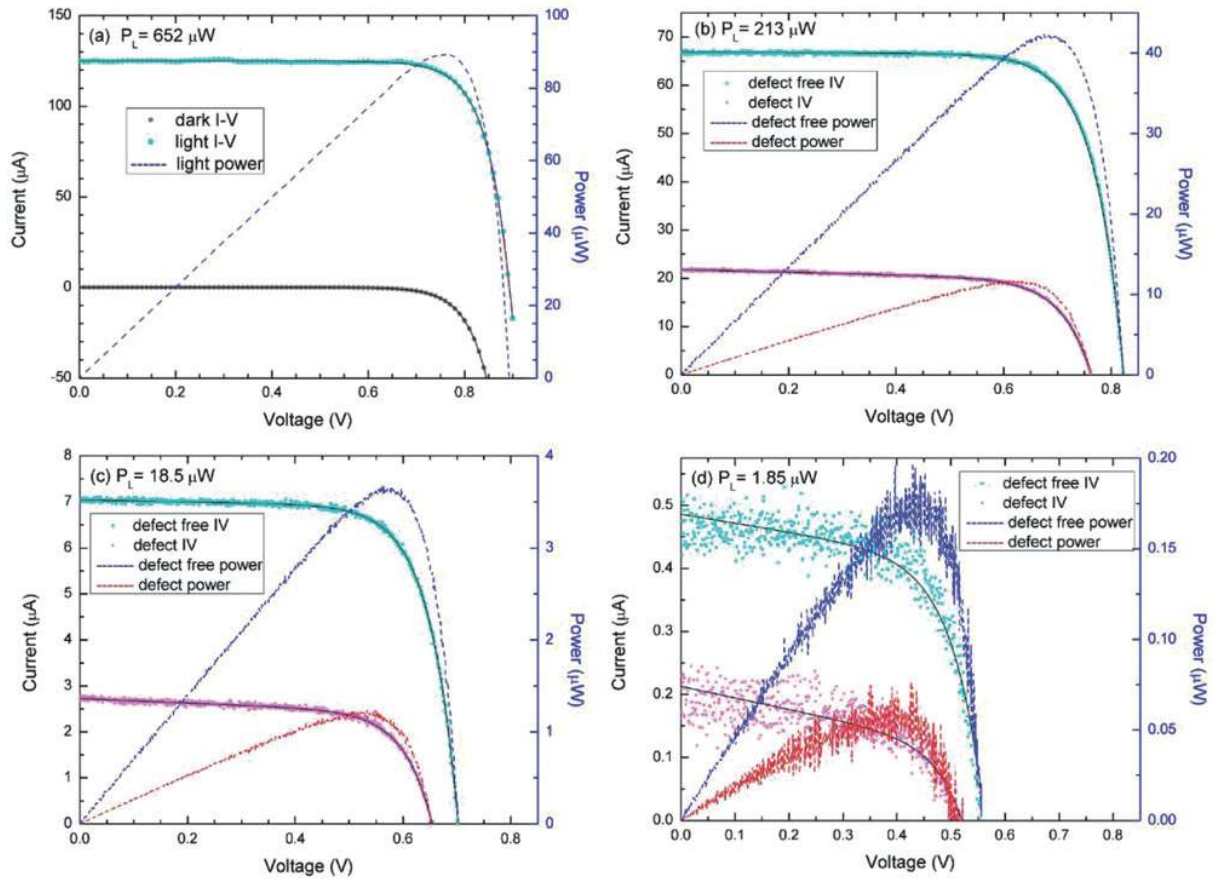
Fig. 4. (Color online) Impact of a defect on solar cell characteristic: left axes for $I–V$ curves (discrete points are experimental data, black solid curves are fitting results), right axes for $P–V$ curves (calculated from experimental data). (a) Cell #5 illuminated under approximate one sun. (b–d) Comparison between a defect-free site and defect site #5-2A, illuminated with a 532 nm focused laser beam under three different laser powers. (reproduced with permission[20])

man signal results from the coupled mode of the LO phonon and plasmon (LOPP)[28], the lower carrier density at the defect site makes its Raman spectrum more resembling that of the intrinsic GaAs.

2.3. Microscopic *I–V* measurements under illumination at defect sites

A dark $I–V$ characteristic reflects the average property of the device, which obviously cannot probe individual defects. However, under the illumination of a focused beam, the inhomogeneity of the device can be investigated. By raster scanning the laser beam while monitoring the short-circuit current of a PV cell, one can have a so-called laser-beam-induced current (LBIC) map[22]. One can further park the laser beam at one location to measure the light $I–V$ characteristic. Such obtained light $I–V$ characteristic can be rather similar to that of the light $I–V$ characteristic of the cell as a whole illuminated by light, as in the case of the GaAs solar cells that were studied. However, for the CZTSe thin-film cells studied previously[22], it was found that local light $I–V$ curves were very different from that of the whole cell light $I–V$ curve.

It is not always possible to make direct comparison between the macroscopic and microscopic $I–V$ characteristics. The reason is that the device is operated under very different conditions between the two cases. Only a very small area is illuminated in the microscopic measurement, which is approximately equivalent to a solar cell with a small active area that is under illumination and a large electrode area, the

whole non-illuminated area, that is under forward bias, thus resulting in much higher dark current. Hence, the microscopic light $I–V$ curve tends to show reduced V_{oc} and FF, which was very significant for the CZTSe cells[22] but much lesser in the GaAs devices, because the latter had an overall lower dark current and a larger shunt resistance than other thin-film solar cells.

Fig. 4 shows the microscopic light $I–V$ characteristics measured at the location of the largest defect #5-2A identified in Fig. 3(a) under different illumination powers. For reference, the light and dark $I–V$ curves for cell #5 as a whole are shown in Fig. 4(a). The dark $I–V$ curve indicates a well-behaved diode characteristic. The light $I–V$ curve is obtained using a solar simulator with a power density of 850 W/m², which gives rise to $I_{sc} = 0.125$ mA, $V_{oc} = 893$ mV, and $P_{max} = 0.0892$ mW. Using the total active device area (the sum of all the strips) of 0.767 mm² or $P_L = 0.652$ mW, the energy conversion efficiency of this small cell is $\eta = P_{max}/P_L = 13.7\%$, and the fill factor is FF $= P_{max}/(I_{sc}V_{oc}) = 0.799$. Figs. 4(b)–4(d) show results obtained using a 532 nm focused laser beam (with a 50xLWD/ND0.5 lens) under three laser powers (roughly over three orders in magnitude), $P_L = 213$, 18.5, and 1.82 μW, respectively. Key cell parameters were calculated from the measured data given in Table 1.

All cell parameters are found to degrade at the defect site, regardless of the illumination power level, but the extent of degradation depends on the illumination density. From the high to low power, the reductions in efficiency are

Table 1.   Summary of characterization results for defect #5-2A. The first row is for the macroscopic results of #5 as a whole, measured under approximate 1 sun (~850 W/m²). The remaining rows are microscopic results measured using a diffraction-limit laser beam of 532 nm. The error bars are given as superscripts for the key parameters. The efficiency values in parentheses have been corrected for the reflectance loss ($R = 0.29$ @532 nm). (reproduced with permission[20])

P_L (μW)	Site	I_{sc} (μA)	V_{oc} (mV)	FF	η (%)	I_0 (pA)	n	R_{sh} (MΩ)	R_s (10^{-3} Ω)
652	Whole cell	125 ± 0.2	893 ± 0.1	0.799 ± 0.003	13.7 ± 0.1(~19.3)	0.778	1.83	4.75	0.90
213	Defect-free	66.9 ± 0.3	822 ± 0.5	0.766 ± 0.007	19.8 ± 0.1(27.9)	17.9	2.11	1.57	3.93
	Defect	21.7 ± 0.3	762 ± 0.5	0.708 ± 0.02	5.49 ± 0.1(7.73)	20.1	2.15	0.356	3.82
18.5	Defect-free	7.03 ± 0.02	701 ± 0.5	0.728 ± 0.011	19.4 ± 0.2(27.3)	11.1	2.04	4.76	1.71
	Defect	2.72 ± 0.02	655 ± 0.5	0.674 ± 0.022	6.49 ± 0.16(9.14)	7.88	2.01	2.08	6.43
1.82	Defect-free	0.468 ± 0.04	556 ± 2	0.653 ± 0.067	9.34 ± 0.55(13.2)	21.0	2.21	7.09	4.82
	Defect	0.194 ± 0.04	510 ± 8	0.546 ± 0.146	2.97 ± 0.44(4.18)	5.11	2.05	5.08	2.83

72.3%, 66.5%, and 68.2%, respectively, for the three laser powers. For this particular defect, the variation in the magnitude of efficiency reduction does seem to depend on the illumination density. Because the laser spot size is much larger than the defect core, the I–V characteristic of the "defect site" actually reflects an average effect within the laser spot size which is comparable to the lateral carrier diffusion length in this device. These results provide semi-quantitative assessment of the impact of an individual defect in a solar cell. However, it is non-trivial to evaluate the impact of an individual defect exactly in a device, which depends on the impacted area relative to the total illuminated area. Despite the significant efficiency reductions, the ratios are nevertheless much smaller than those in PL, because PL is measured under the open-circuit condition where the nonradiative recombination is much more competitive than the radiative recombination. In fact, the GaAs materials comparable to the one used in this solar cell exhibited relatively low internal quantum efficiency in PL at the low excitation density (e.g., 1 sun)[6], but they could, however, yield reasonably good cell efficiencies, benefiting from the strong carrier extraction power under the non-open-circuit condition.

The light I–V characteristic of a well-behaved solar cell can be described by the standard model[29]:

$$I = I_L - I_0\left(e^{\frac{q(V+IR_s)}{nkT}} - 1\right) - \frac{V + IR_s}{R_{sh}}, \qquad (1)$$

where I_L is the photo-generated current, I_0 is the dark reverse saturation current, V is the photo-voltage generated by the solar cell, n is the diode ideality factor ($n = 1$ for an ideal diode), R_{sh} is the shunt resistance (ideally infinity), and R_s is the series resistance (ideally zero). Additionally, q is the electron charge, k is the Boltzmann's constant, and T is the absolute temperature. Eq. (1) is not, strictly speaking, applicable for the focused illumination. However, since the obtained I–V curves under focused illumination appear similar to a typical well-behaved solar cell, they can be fitted well using Eq. (1). The fitting curves are plotted in Figs. 4(b)–4(d), and show excellent agreement with the measured data. The effective n, R_{sh} and R_s values are obtained from the fitting, and are listed in Table 1. Quantitative comparisons of I_0 and n between either uniform and focused illumination or defect-free and defect site are not straightforward to make, other than noting that I_0 is significantly larger for focused illumination, because the dark area is much larger for the latter case. A more important finding between the defect-free and defect sites is that the latter

consistently yields lower shunt resistance under the same illumination power, and more so for higher illumination power. This trend can be explained as follows: firstly, the dislocation defect provides a shunt to the photogenerated carriers; secondly, the effect is more significant for high excitation density, because the effect of the point defects is saturated, and the dislocation defect becomes more prevalent[5, 7, 25].

2.4. Impact variation for different defects

Several threading dislocation defects were characterized by PL, Raman, and I–V characteristic under the same conditions, as shown in Fig. 5, where the results are compared for the three neighboring defects shown in Fig. 3(c), #5-2A, #5-2B, and #5-2C, and another defect, #5-3A, from area #5-3. Figs. 5(a) and 5(b) are, respectively, the PL and Raman mapping results near defect #5-2B & C. Figs. 5(c) and 5(d) are the same results for defect #5-3A, and they are qualitatively similar to the corresponding results for #5-2A, Figs. 3(c) and 3(e). Figs. 5(e) and 5(f) compare, respectively, the PL and Raman spectra of the four defects and the defect-free site. Evidently, as shown in Fig. 5(e), the PL peak positions of the GaAs peak are rather different for different defects, but all are blue-shifted from the defect-free value: 858–867 nm or $\delta E = 17$–2 meV relative to 868 nm of the defect-free site. Within #5-2A, #5-2B, and #5-2C, the amount of reduction in PL intensity seems to correlate with the visual size of the defect with the largest defect #5-2A, shown in Fig. 3(c), also exhibiting the most intensity reduction. Fig. 5(f) compares the Raman spectra of the four defects. There is qualitatively an anti-correlation between the PL intensity and LO mode Raman intensity among the four defects, which can be explained by the opposite dependencies of the carrier density for PL and Raman [26]. Figs. 5(g) and 5(h) depict their I–V characteristics under two illumination powers (2.1 and 225 μW) for comparison between the four defects. The severity of impact is in the order of A, B, and C, with A being the strongest for the three defects in area #5-2, whereas the impact for #5-2A and #5-3A are comparable.

2.5. Correlative structural characterization of
individual defects

Once optical and optoelectronic characterization of individual defects are completed, the next logical step is to investigate the microscopic structure of the same defects. However, this specific step has rarely been taken in the past defect research. In our study, the defect locations, defined as the lowest PL intensity positions, were carefully noted under
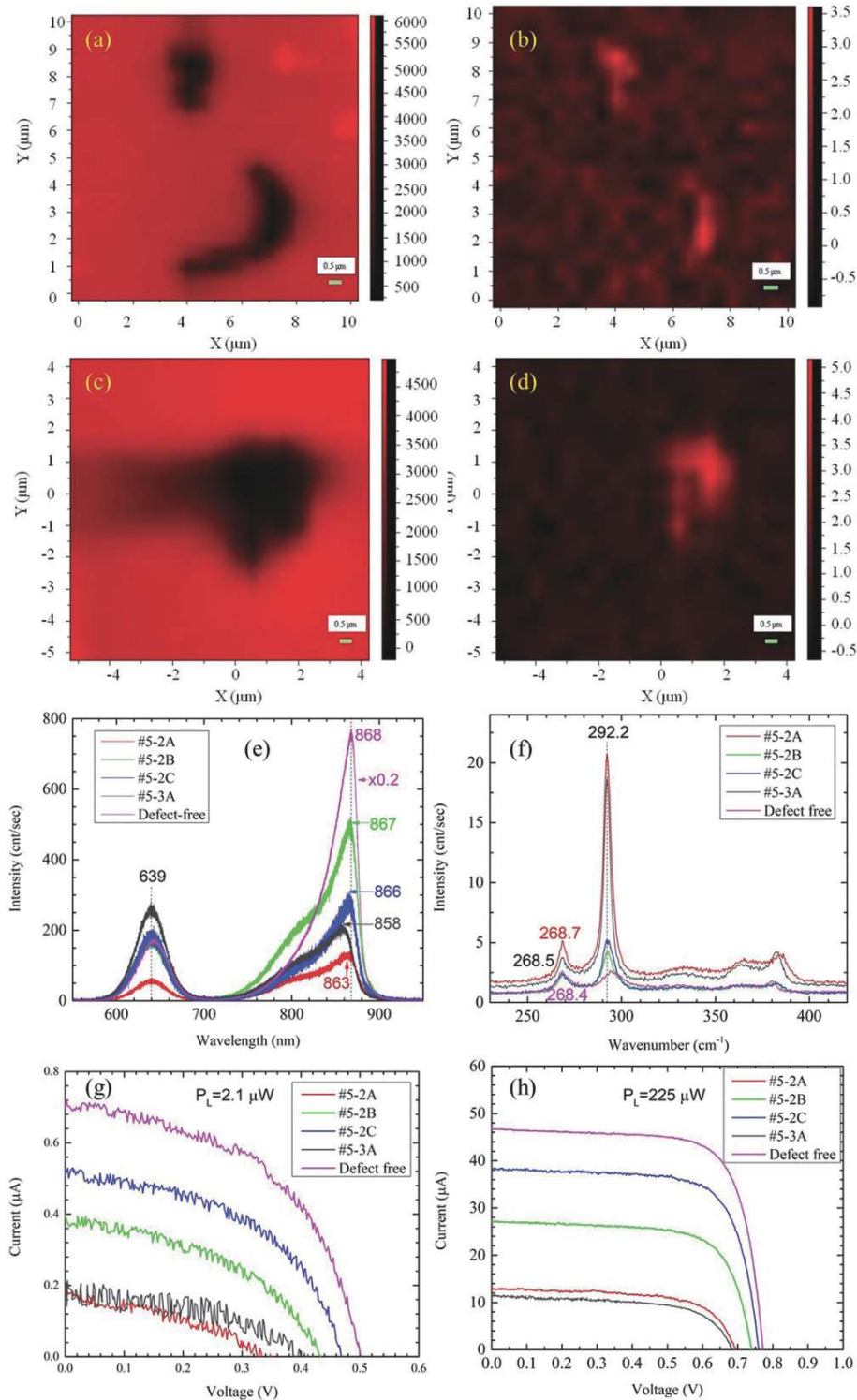
Fig. 5. (Color online) Comparison of different defects. (a, b) PL and Raman mapping of defect #5-2B and #5-2C. (c, d) PL and Raman mapping of defect #5-3A. (e, f) PL and Raman spectra of defect #5-2A-C and #5-3A, and a defect-free site. (g, h) The same in *I–V* characteristic under two illumination powers. (reproduced with permission[20])

high magnification optical microscope imaging (with about 0.1 *μ*m accuracy), typically with respect to some nearby recognizable surface feature, so that they could be located again using the SEM in the dual-beam FIB system that was used for preparing the cross-sectional TEM samples. Several defects were investigated. Results are highlighted here for two of them: #5-2A and #5-3A.

Fig. 6 shows low magnification TEM and atomically-resolved scanning TEM images of #5-2A. The PL image in Fig.

3(c) had already indicated that this defect was laterally more extended than most of the other defects. A thin specimen slice was extracted using the FIB milling system, from the device at the approximate location indicated on the PL image included with Fig. 6(a). This image reveals that this defect cluster is mostly confined to the GaAs emitter layer and penetrates only a short distance downwards into the GaAs absorber layer, although it extends laterally by more than one micron. However, the GaInP window layer above the GaAs lay-

Y Zhang et al.: Comprehensive, *in operando*, and correlative investigation of defects and their impact ......
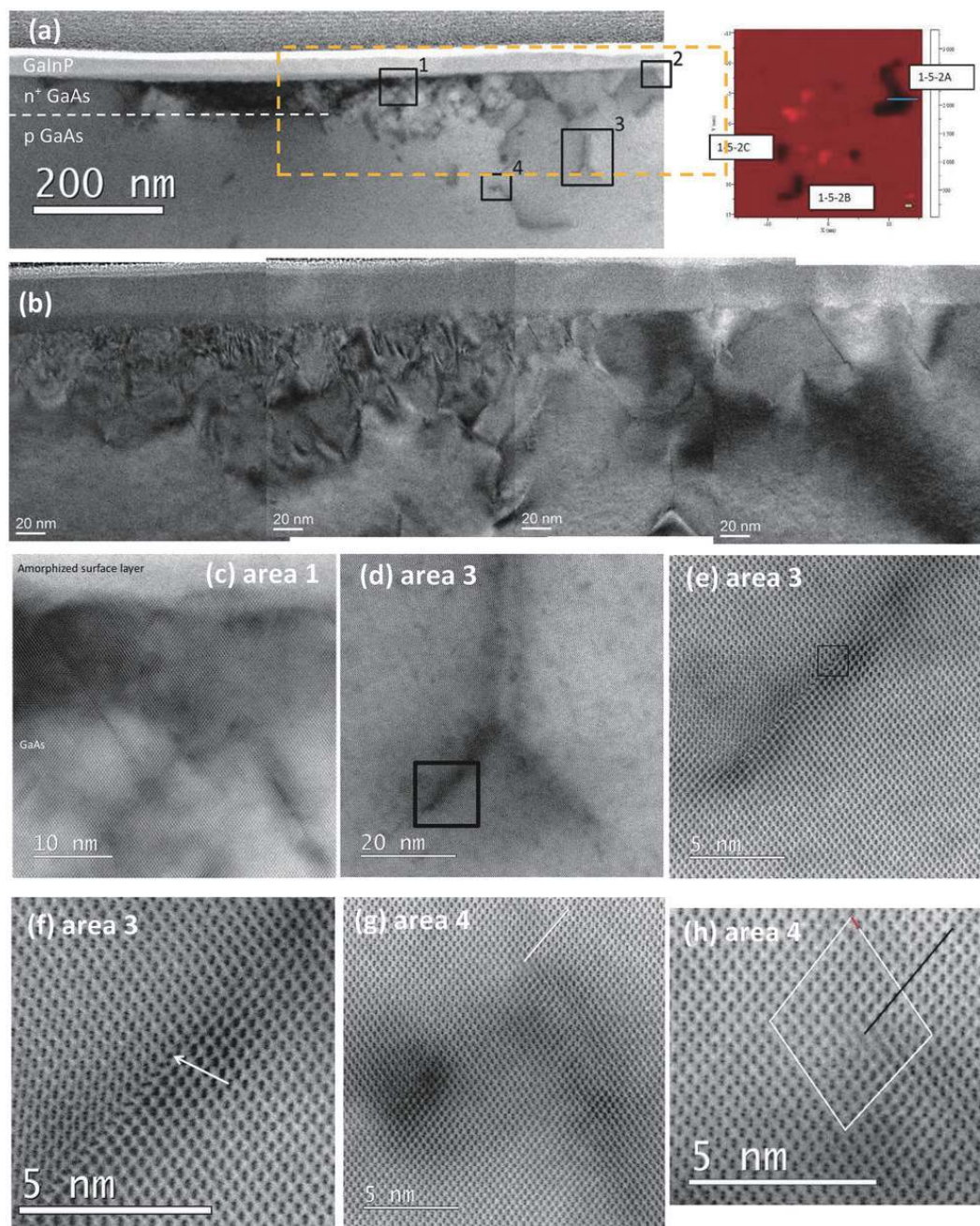
Fig. 6. (Color online) TEM images of defect #5-2A. (a) Low magnification image of defective region. (b) Enlargement taken from the area indicated by the yellow box in (a). (c–h) High-resolution images of areas indicated in (a): (c) from area 1; (d–f) from area 3 with different magnification, where in (e) the end of the stacking fault marked by a black square ends in a 30° partial dislocation while the other end terminates in a 90° partial dislocation, and in (f) enlarged view of the area marked by the black square has a single atomic column of arsenic atoms at the core of the 30° partial dislocation (marked by white arrow). (g, h) from area 4: (g) 60° dislocation near top of the image. The extra half-plane of paired columns is indicated with a white line. (h) Enlarged view of 60° dislocation in (g). Burgers circuit is shown in white with the resulting Burgers vector shown in red. The extra half-plane is marked in black. (reproduced with permission[20])

er in this region seems to be free of defects, as shown in Fig. 6(b), which is an enlargement of the region indicated by the yellow box in Fig. 6(a). This defect is clearly a massive cluster combining many individual defects. Some of these areas were examined more closely, and high-resolution images were taken from the four areas indicated in Fig. 6(a). Areas 1 and 2 include the GaInP/GaAs interface. The structures of the area 1 and 2 are similar, as shown in Fig. 6(c) for area 1, which indicates that the top region of the device (part of the GaInP window layer) is amorphized. The area 3, shown enlarged in Figs. 6(d)–6(f), has a stacking fault, where the end of

the stacking fault marked by a black square in Fig. 6(e) ends in a 30° partial dislocation while the other end terminates in a 90° partial dislocation. An enlarged view is given in Fig. 6(f). According to detailed analysis of a high-angle annular-dark-field (HAADF) STEM image of the same area (not shown here), the single atomic column at the core of the 30° partial dislocation (marked by the white arrow) consists of arsenic. Area 4, as shown in Figs. 6(g) and 6(h), exhibits a 60° dislocation near the top of the image, and the extra half-plane of paired columns is indicated by the white line in Fig. 6(g). An enlarged view of this dislocation is shown in Fig. 6(h): the Bur-
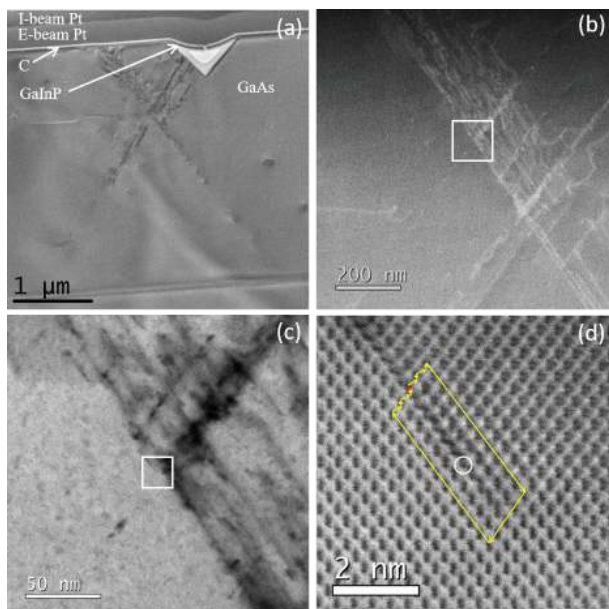
Fig. 7. (Color online) TEM images of defect #5-3A. (a) Low magnification image of defective region (note the triangular-shaped pit beneath sample surface adjacent to the defect cluster); (b) HAADF image, and (c) LABF image, showing major intersection of stacking defects and dislocations; (d) Aberration-corrected LABF STEM image of an intrinsic stacking fault terminated by a 30° partial dislocation as identified by the Burgers' circuit shown in yellow. Single As atomic column (circled) at the defect core. (reproduced with permission[20])

gers circuit is shown in white, with the resulting Burgers vector shown in red. The extra half-plane of atoms is marked with the black line.

Fig. 7 shows the results of the microscopic characterization of defect #5-3A, which is structure-wise distinctly different from #5-2A, and has been shown to have comparable impact on the optical properties and device performance (Fig. 5). In the optical image of the device (not shown), there is a white spot right next to the EL dark spot at defect #5-3A. The low-resolution TEM image in Fig. 7(a) reveals that the white spot corresponds to a pit-like feature in GaAs near the device surface, which is covered over by the GaInP window layer, while the dark spot in the EL map is caused by the defect cluster adjacent to the pit. This defect cluster extends mostly along {111}-type directions from the surface of the solar cell down into the absorber material for at least 2 μm, but not apparently all the way through to the back-surface confinement layer. However, it is far less extended laterally compared to #5-2A. It includes many structural defects, which are mostly concentrated in the top 1 μm of the absorber layer. Fig. 7(b) is a HAADF image showing a major intersection of defect clusters and Fig. 7(c) is a corresponding large-angle BF (LABF) image taken at higher magnification. Fig. 7(d) is a LABF STEM image of the area in the white square in Fig. 7(c), and shows a single 30° partial dislocation that terminates an intrinsic stacking fault. The dislocation type is identified in Fig. 7(d) by drawing a Burgers circuit around the defect, as shown by the red arrows. The resulting projected Burgers vector is indicated by the red arrow. The extended stacking fault is terminated by a single, unpaired atomic column indicated by the white circle in the figure, which is identified as corresponding to As.

Each of the defect clusters was unique, yet they shared common characteristics. Visual comparison of the different defect clusters showed that every cluster was dominated by a collection of extended {111}-type stacking faults, mostly located near the top of the device in the GaAs emitter and absorber layers. In contrast to the common belief that dislocation defects in the GaAs epilayer originate from the substrate that happens to have a comparable defect density, these defects were typically initiated within the absorber layer at around 0.5 to 1.5 μm from the lower GaAs/GaInP interface, and passed through the GaAs emitter and the GaInP window layer. However, one defect cluster (#5-2A), with relatively short stacking faults, remained mostly confined to the n$^+$ GaAs emitter layer, leaving the GaInP window layer nearly free of defects, and only extended down into the GaAs absorber layer over a short distance (~0.25 μm). It might seem counter-intuitive that the GaInP PL signal is often weaker from the non-defective GaInP site (#5-2A) than from the defective GaInP site (#5-3A), as shown in Fig. 5(e). The explanation could be that the carriers in the former case are mostly captured by the underneath GaAs layer, whereas the carriers are localized to the GaInP layer itself in the latter case.

Although we did not observe significant change (enhancement) of the TO mode intensity at the defect site, as previously suggested resulting from relaxation in selection rule due to defect induced disordering[30, 31], we observed a strongly enhanced TO Raman mode at the location of the pit, shown in Fig. 7(a), which has {111}-like surfaces for which TO Raman scattering is allowed. We note that the lateral extensions of the defects identified in these epitaxially-grown solar cells are much smaller than the dislocation defects observed in GaAs ingots, which are intended to be used as substrates, with lateral sizes in the order of 100 μm[30, 31]. Moreover, dislocation defects originated from the substrate, e.g., in SiC[19], are often found to be much larger in lateral size.

Overall, these observations reveal that those defects showing major impact on optoelectronic performance (e.g., reduction in PL intensity and photo-current) were most often associated with a cluster of extended defects rather than a single extended defect, as previously assumed based on optical data alone. Those extended defects that exhibited weaker impact on the material properties and device performance have not been carefully examined. Quite likely they were simpler defects, which remain to be investigated.

One further step towards advancing this correlative approach to defect characterization would naturally be to perform density-functional theory (DFT) level structural and electronic calculations using the HRTEM results as inputs. However, realistically, the defect complexes, such as those discussed above (e.g., #5-2A and #5-3A), are too challenging for the most capable DFT codes to deal with at this time. Nevertheless, one could begin with those well-defined sub-structures for the defect modeling.

The series approach illustrated above has provided unique and unprecedent insights for both practical knowledge of the adverse effects of defects and fundamental understanding of defect physics at the single defect level. The impact of the dislocation defect on the solar cell performance parameters tends to be more significant at higher illumination density, because of the competing roles of point and ex-
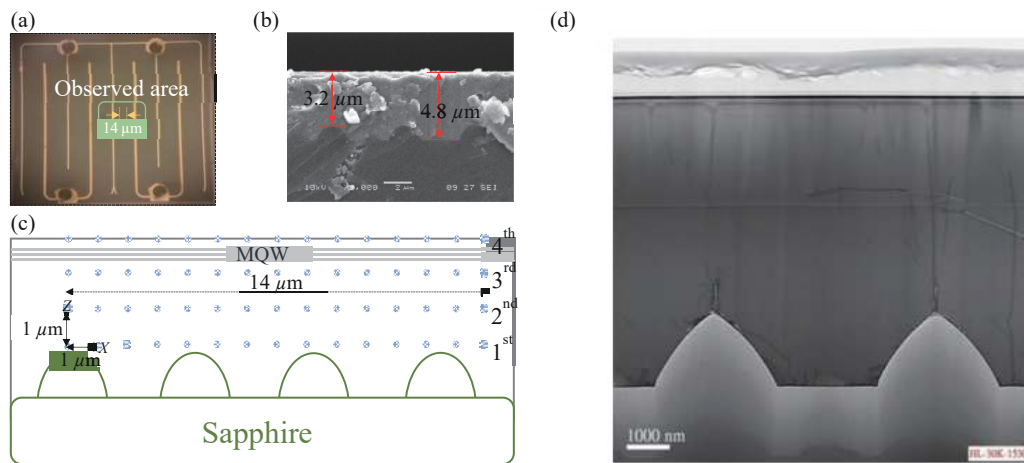
Fig. 8. (Color online) Top and cross-sectional images of the LED, and temperature probing points on the device cross section. (a) Top view of optical microscope image, (b) cross-sectional SEM image, (c) cross-sectional schematic drawing showing the measured locations (blue dots) at four different depths, and (d) a cross-sectional TEM image from a similar device. (reproduced with permission[24])

tended defects. In addition to reduction in photo-current and open-circuit voltage, the dislocation defects also reduce the shunt resistance, due to enhanced recombination loss through the defect states. The degree of impact varies significantly among different defects, and the trend is mostly consistent between the spectroscopy signatures (e.g., PL intensity) and optoelectrical characteristics (e.g., *I–V* characteristic). In the future, the same approach can be used to probe devices under high injection current or high illumination density to induce structural modifications of the defects, and then to investigate the effects.

3. 3-D Raman thermometry for device characterization

Several techniques are available to measure device temperature, from perhaps the most straightforward method – IR imaging[32] to more sophisticated methods, such as lock-in thermography[33], thermo-reflectance[34], and Raman thermometry[35]. These techniques are typically only capable of or were only used for probing the surface temperature of a device. An *in operando* micro-Raman based 3-D thermometry has recently been developed with diffraction-limit spatial resolution and high temperature accuracy of ± 2 $^\circ$C[24]. While measuring Raman signal from the volume below the device surface is not difficult with a confocal micro-Raman system when a below bandgap laser is used, the salient aspect of this technique is its ability to suppress the interference of the below bandgap emission of an InGaN LED when it is operated under CW injection. The general idea of the technique is to drive LEDs under a continuous current for a relatively long period of time to allow the device to reach a steady operational state, then switch the power off briefly to take the Raman spectrum in the middle of the off-time window. This "split-time-window" method takes advantage of the fact that the electronic relaxation time is much faster than the thermal relaxation time so that the luminescence decays quickly after the device is turned off but the thermal distribution remains nearly the same as in a truly continuous mode during the Raman data collection window. Additionally, in the past, Raman frequency shift was often used as a temperature calibration, which could be problematic, because temperature change also leads to stress relaxation that also contributes to

the Raman frequency shift. Therefore, the calibrated relative intensity ratio of Stokes and anti-Stokes Raman scattering is used as the temperature metric in the new approach.

Fig. 8 shows the LED device and the 3-D locations that were measured in this demonstration. Fig. 8(a) shows the optical image of the device, and Fig. 8(b) the cross-section SEM image. As shown schematically in Fig. 8(c), a total of 60 locations were measured on one vertical cross section area at different depths from the sapphire substrate/GaN buffer layer interface to the top surface of the device.

The results are shown in Fig. 9 under 350 mA current (for a 1 mm size LED chip). Fig. 9(a) depicts the measured temperature contour in the *x–z* cross section. The overall temperature profile looks like a columnar shape along the vertical direction. Assuming the LED junction temperature is the same as the top surface temperature, we find that at 350 mA the average temperature difference is only approximately 2 $^\circ$C between the top and bottom of the GaN epilayer, as shown in Fig. 9(b). However, we note that the magnitude of temperature fluctuation within the same depth can be significantly larger than the overall laterally averaged variation in the depth direction, because for various reasons the device simply does not have an axial symmetry to justify treating it as a 1-D system. Within the cross section, the maximum temperature of 86.2 $^\circ$C (location no. 4) is measured at the top surface and a minimum temperature of 74.8 $^\circ$C (no. 1) is measured at the bottom surface close to the sapphire substrate. Raman spectra of a few extreme points (no. 1 to no. 4) are included in Fig. 9(a). Moreover, we find that, despite some fluctuation, on average the GaN temperature near the top of the patterned sapphire pillars is lower than that of the region between the top sites at the same height. Fig. 9(c) plots the temperatures from 32 locations for each of the two types of sites and the averaged difference is approximately 5.7 $^\circ$C. We note that the density of the hot spots is much lower than the typical defect density in this type of material, as shown by the TEM image from a similar device, Fig. 8(d).

Clearly it is of great interest to further investigate the microscopic structure of the identified hot spots using HRTEM, as we have done for GaAs solar cells to correlate the spatially resolved optoelectronic characterization with structural analysis[20]. One can continue monitoring the temperature distribu-
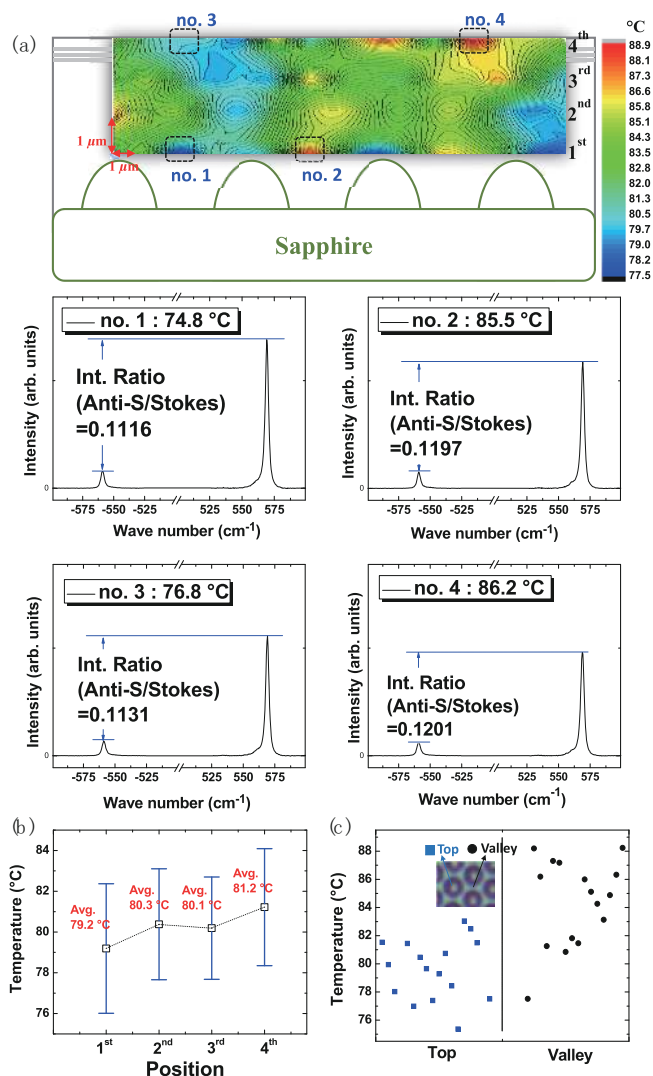
Fig. 9. (Color online) 3D temperature profile sampling results. (a) Cross-sectional temperature contours calculated from the intensity ratio of Stokes and anti-Stokes Raman scattering and Raman spectra of a few extreme points (no. 1 to no. 4) below. (b) Average temperatures at different depths. (c) Scattered plots of temperatures at two types of sites ("top" and "valley") at the first depth. (reproduced with permission[24])
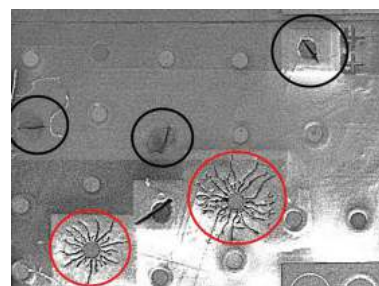

Fig. 10. (Color online) Plan-view SEM image showing two distinct failure modes in GaN power devices stressed to breakdown: i) Black: deep cracks and surface crater; ii) Red: cracks branching out from device.

we should be able to directly monitor development of the current leakage process and identify the underlying cause(s). Moreover, by continuously measuring the relevant physical parameters at locations showing excessive temperature rise, it should be possible to determine the critical point when irreversible damage occurs.

4. Concluding remarks

Using GaAs solar cells as prototype devices, we have demonstrated how a series approach to device characterization, which offers comprehensive, *in operando* and correlative information about defects in a semiconductor device, can lead to answers to the important questions that would otherwise never be answered with certainty. We anticipate that this novel approach, coupled with the various spatially-resolved characterization techniques described in this review, can be more broadly applied to investigate the physics of defect and the roles that they play in real devices under different operation conditions, and to assess practical device reliability issues.

Acknowledgements

References

[1] Kittel C. Introduction to solid state physics. John Wiley & Sons, Inc, 2005

[2] Lannoo M, Bourgoin J. Point defects in semiconductors I. Berlin, Heidelberg: Springer Berlin Heidelberg, 1981

[3] Bourgoin J, Lannoo M. Point defects in semiconductors II. Berlin, Heidelberg: Springer Berlin Heidelberg, 1983

[4] Holt D B, Yacobi B G. Extended defects in semiconductors. Cambridge: Cambridge University Press, 2007

[5] Gfroerer T H, Zhang Y, Wanlass M W. An extended defect as a sensor for free carrier diffusion in a semiconductor. Appl Phys Lett, 2013, 102, 012114

[6] Zhang F, Castaneda J F, Chen S S, et al. Comparative studies of optoelectrical properties of prominent PV materials: Halide perovskite, CdTe, and GaAs. Mater Today, 2020, 36, 18

[7] Lin Y, Zhang Y, Liu Z Q, et al. Interplay of point defects, extended defects, and carrier localization in the efficiency droop of InGaN quantum wells light-emitting diodes investigated using spatially resolved electroluminescence and photoluminescence. J Appl Phys, 2014, 115, 023103

[8] Petroff P, Hartman R L. Defect structure introduced during opera-

tion to even higher injection current to assess the device failure mechanism, as well as measure the temperature effect of the spatially resolved efficiency droop[36].

The 3-D Raman thermometry is equally applicable to other devices, such as monitoring highly non-uniform heating, potentially the failure mechanism, in power electronic devices. More effectively, one can apply a similar correlative approach demonstrated for the GaAs solar cells to power electronic devices based on III-nitrides, SiC, and Ga_2O_3, which likewise face device fabrication, performance, and reliability challenges related to extended defects. For example, we recently observed the morphology of failed GaN-on-GaN vertical p–i–n diode devices after reverse-bias electrical stressing to breakdown, and found large surface craters that were ~15–35 μm deep with lengthy surface cracks, and substantial concentrations of threading dislocations around the cracks and near the crater surfaces[37]. Moreover, as illustrated in Fig. 10, we have recently found two different breakdown mechanisms in stress-tested devices. By applying the proposed methodology to GaN power devices during biasing and stress testing,

tion of heterojunction GaAs lasers. Appl Phys Lett, 1973, 23, 469

[9]   Kurtsiefer C, Mayer S, Zarda P, et al. Stable solid-state source of single photons. Phys Rev Lett, 2000, 85, 290

[10] Francoeur S, Klem J F, Mascarenhas A. Optical spectroscopy of single impurity centers in semiconductors. Phys Rev Lett, 2004, 93, 067403

[11] Romero M J, Du H, Teeter G, et al. Comparative study of the luminescence and intrinsic point defects in the kesterite Cu_2ZnSnS_4 and chalcopyrite Cu(In, Ga)Se$_2$ thin films used in photovoltaic applications. Phys Rev B, 2011, 84, 165324

[12] Alberi K, Fluegel B, Moutinho H, et al. Measuring long-range carrier diffusion across multiple grains in polycrystalline semiconductors by photoluminescence imaging. Nat Commun, 2013, 4, 2699

[13] Liu H N, Zhang Y, Chen Y P, et al. Confocal micro-PL mapping of defects in CdTe epilayers grown on Si (211) substrates with different annealing cycles. J Electron Mater, 2014, 43, 2854

[14] Fluegel B, Alberi K, DiNezza M J, et al. Carrier decay and diffusion dynamics in single-crystalline CdTe as seen via microphotoluminescence. Phys Rev Applied, 2014, 2, 034010

[15] Kuciauskas D, Myers T H, Barnes T M, et al. Time-resolved correlative optical microscopy of charge-carrier transport, recombination, and space-charge fields in CdTe heterostructures. Appl Phys Lett, 2017, 110, 083905

[16] Xu X, Beckman S P, Specht P, et al. Distortion and segregation in a dislocation core region at atomic resolution. Phys Rev Lett, 2005, 95, 145501

[17] Smith D J, Aoki T, Mardinly J, et al. Exploring aberration-corrected electron microscopy for compound semiconductors. Microscopy, 2013, 62, S65

[18] Li C, Wu Y L, Pennycook T J, et al. Carrier separation at dislocation pairs in CdTe. Phys Rev Lett, 2013, 111, 096403

[19] Hauer B, Marvinney C E, Lewin M, et al. Exploiting phonon-resonant near-field interaction for the nanoscale investigation of extended defects. Adv Funct Mater, 2020, 30, 1907357

[20] Chen Q, McKeon B S, Zhang S Y, et al. Impact of individual structural defects in GaAs solar cells: A correlative and in operando investigation of signatures, structures, and effects. Adv Opt Mater, 2021, 9, 2001487

[21] Chen Q, McKeon B S, Becker J, et al. Correlative characterization of dislocation defects and defect clusters in GaAs and CdTe solar cells by spatially resolved optical techniques and high-resolution TEM. 2018 IEEE 7th World Conference on Photovoltaic Energy Conversion, 2018, 3234

[22] Chen Q, Zhang Y. The reversal of the laser-beam-induced-current contrast with varying illumination density in a $Cu_2ZnSnSe_4$ thin-film solar cell. Appl Phys Lett, 2013, 103, 242104

[23] Lin C H, Merz T A, Doutt D R, et al. Strain and temperature dependence of defect formation at AlGaN/GaN high-electron-mobility transistors on a nanometer scale. IEEE Trans Electron Devices, 2012, 59, 2667

[24] Park T, Guan Y J, Liu Z Q, et al. In operando micro-Raman three-dimensional thermometry with diffraction-limit spatial resolution for GaN-based light-emitting diodes. Phys Rev Appl, 2018, 10, 034049

[25] Chen F, Zhang Y, Gfroerer T H, et al. Spatial resolution versus data acquisition efficiency in mapping an inhomogeneous system

with species diffusion. Sci Rep, 2015, 5, 10542

[26] Hu C, Chen Q, Chen F, et al. Overcoming diffusion-related limitations in semiconductor defect imaging with phonon-plasmon-coupled mode Raman scattering. Light Sci Appl, 2018, 7, 23

[27] Irmer G, Wenzel M, Monecke J. Light scattering by a multicomponent plasma coupled with longitudinal-optical phonons: Raman spectra of p-type GaAs:Zn. Phys Rev B, 1997, 56, 9524

[28] Mooradian A, Wright G B. Observation of the interaction of plasmons with longitudinal optical phonons in GaAs. Phys Rev Lett, 1966, 16, 999

[29] Green M A. Silicon solar cells. University of New South Wales, Sydney, 1995

[30] Paetzold O, Irmer G, Monecke J, et al. Micro Raman study of dislocations in n-type doped GaAs. J Raman Spectrosc, 1993, 24, 761

[31] Martín P, Jiménez J, Frigeri C, et al. A study of the dislocations in Si-doped GaAs comparing diluted Sirtl light etching, electron-beam-induced current, and micro-Raman techniques. J Mater Res, 1999, 14, 1732

[32] Chang K S, Yang S C, Kim J Y, et al. Precise temperature mapping of GaN-based LEDs by quantitative infrared micro-thermography. Sensors, 2012, 12, 4648

[33] Wu D T, Busse G. Lock-in thermography for nondestructive evaluation of materials. Revue Générale De Thermique, 1998, 37, 693

[34] Dallas J, Pavlidis G, Chatterjee B, et al. Thermal characterization of gallium nitride p-i-n diodes. Appl Phys Lett, 2018, 112, 073503

[35] Senawiratne J, Li Y, Zhu M, et al. Junction temperature measurements and thermal modeling of GaInN/GaN quantum well light-emitting diodes. J Electron Mater, 2008, 37, 607

[36] Lin Y, Zhang Y, Liu Z, et al. Spatially resolved study of quantum efficiency droop in InGaN light-emitting diodes. Appl Phys Lett, 2012, 101, 252103

[37] Peri P, Fu K, Fu H Q, et al. Structural breakdown in high power GaN-on-GaN p-n diode devices stressed to failure. J Vac Sci Technol A, 2020, 38, 063402

Yong Zhang received the Ph.D. from Dartmouth College in Physics in 1994. He was a Senior Scientist at National Renewable Energy Laboratory. He is Bissell Distinguished Professor with ECE Department, UNC-Charlotte, USA. He is an APS Fellow. His research interests include electronic and optical properties of semiconductors and related nanostructures, organic-inorganic hybrid materials, impurity and defects in semiconductors.

David J. Smith received the Ph.D. (1978) and D.Sc. (1988) from the University of Melbourne, Australia. He is currently Regents' Professor with the Department of Physics, Arizona State University, Tempe, USA. His research interests include the development and applications of advanced electron microscopy methods to the study of contemporary materials, including semiconductor heterostructures and many types of nanostructures.